Journal of Orthopaedic Translation 55 (2025) 346–359

Contents lists available at ScienceDirect

Journal of Orthopaedic Translation

journal homepage: www.journals.elsevier.com/journal-of-orthopaedic-translation

Original article

Targeting MAT2A synergistically induces DNA damage in osteosarcoma cells through EZH2-mediated H3K27me3 modification

Binghui Yang [a,b,1], Haoyu Wang [a,b,1], Yining Tao [a,b,1], Xiyu Yang [a,b,1], Haoran Mu [a,b,*], Liu Yang [a,b], Yafei Jiang [a,b], Zhuoying Wang [a,b], Rui Zhang [d], Zhengdong Cai [a,b], Chunxi Yang [c,**], Dongqing Zuo [a,b,***], Yingqi Hua [a,b,****], Wei Sun [a,b,*****]

[a] Department of Orthopaedic Oncology, Shanghai General Hospital, Shanghai Jiao Tong University School of Medicine, Shanghai, China
[b] Shanghai Bone Tumor Institution, Shanghai, China
[c] Department of Orthopaedic Arthroplasty, Shanghai General Hospital, Shanghai Jiao Tong University School of Medicine, Shanghai, China
[d] Department of Orthopedics, Shanghai Sixth People's Hospital, Shanghai, China

ARTICLE INFO

Keywords:
Osteosarcoma
DNA damage
Methionine metabolism
MAT2A
EZH2
H3K27me3

ABSTRACT

Background: Osteosarcoma (OS) is a highly aggressive primary bone tumor with poor outcomes, particularly in metastatic or recurrent cases. Methionine metabolism and histone methylation, such as H3K27me3, play crucial roles in OS progression.
Methods: We analyzed single-cell RNA sequencing (scRNA-seq) data to identify histone methylation and related pathways associated with malignant proliferation OS cells. A high-throughput compound screen was performed to evaluate potential metabolic and epigenetic targets. In vitro and in vivo experiments were conducted to assess the therapeutic potential of MAT2A inhibition, methionine restriction, and EZH2 inhibition.
Results: MAT2A inhibition or methionine restriction reduced H3K27me3 levels, induced DNA damage, and suppressed OS cell growth. Combining MAT2A and EZH2 inhibitors demonstrated synergistic effects in reducing H3K27me3 levels, enhancing DNA damage, and inhibiting OS growth both in vitro and in vivo.
Conclusion: The combination of MAT2A and EZH2 inhibition significantly reduces intracellular H3K27me3 levels by depleting S-adenosylmethionine (SAM) and inhibiting synthetic enzyme activity, thereby inducing DNA damage in osteosarcoma (OS). Methionine-restricted diet combined with EZH2 inhibition effectively suppresses osteosarcoma growth in vivo.
The translational potential of this article: This study highlights the potential of integrating metabolic and epigenetic interventions in OS therapy. Our findings might present a promising therapeutic strategy for chemotherapy-resistance OS.

1. Introduction

Osteosarcoma (OS) is the most common primary malignant bone tumor, primarily affecting children and adolescents [1]. Despite significant advances in surgical techniques and chemotherapy regimens [2], the survival rate for patients with metastatic or recurrent OS remains extremely low [3,4]. Currently, there is a lack of effective clinical therapeutic approaches, highlighting the urgent need to identify alternative therapeutic targets and strategies.

Chemotherapy typically kills tumor cells by inducing DNA damage in

* Corresponding authors.
** Corresponding authors.
*** Corresponding authors.
**** Corresponding author.
***** Corresponding author. Department of Orthopaedic Oncology, Shanghai General Hospital, Shanghai Jiao Tong University School of Medicine; Shanghai Bone Tumor Institution, 100 Haining Road, 200080, Shanghai, China.
E-mail addresses: dr_muhaoran@163.com (H. Mu), chunxi_yang@163.com (C. Yang), dongqing.zuo1@shgh.cn (D. Zuo), hua_yingqi@163.com (Y. Hua), viv-sun@sjtu.edu.cn (W. Sun).
[1] These authors contributed equally.

https://doi.org/10.1016/j.jot.2025.09.007
Received 24 February 2025; Received in revised form 15 August 2025; Accepted 10 September 2025

clinical tumor therapy. Mechanisms of DNA damage include DNA strand breaks [5,6], R-loop formation [7–10], chromosomal fragmentation, loss of DNA repair enzymes, homologous recombination defects, and targeting DNA damage repair pathways. Synthetic lethality (e.g., BRCA, PRMT5) represents a mechanism capable of precisely inducing DNA damage in tumor cells with specific vulnerabilities. For instance, CIP2A has emerged as a promising synthetic lethal therapeutic target for BRCA1-and BRCA2-mutated cancers [11], while PRMT5 inhibition leads to RPA depletion and impaired homology-directed DNA repair (HDR) activity [12]. However, such approaches are often not universally effective, and existing methods generally lack specificity [13]. Consequently, there may be other biological mechanisms that enable OS cells to overcome DNA damage caused by drugs, allowing them to maintain rapid proliferation [14,15]. Chemotherapy resistance frequently leads to tumor recurrence or metastasis. Studies have shown that recurrent or metastatic tumor tissues undergo significant phenotypic changes, such as increased chemoresistance and accelerated proliferation, compared to pre-treatment tissues, despite showing no significant changes in their genomic characteristics [16,17]. This suggests that epigenetics may play a crucial role in enabling tumor cells to tolerate DNA damage.

Cellular phenotype remodeling without altering the genetic material itself usually is referred to epigenetics. Epigenetics referred to stable changes in cell phenotype on the basis of other than genetic changes [18], such as histone modifications and DNA methylation. The silencing of DNA repair-related genes has been linked to changes in histone methylation levels [19]. For example, Gardner et al. found that EZH2 induces chemotherapy resistance in small-cell lung cancer by upregulating H3K27me3 levels, which suppresses SLFN11 expression [16]. Chang et al. revealed that IOX-1 increases histone H3 trimethylation and ATP-binding cassette transporter expression, which may sensitize MG63 cells to cisplatin [20]. Additionally, epigenetics is also important in OS progression. Jiang et al. demonstrated that H3K27me3 demethylation mediated by KDM6B promotes oncogenic LDHA expression, thereby enhancing OS cell migration in vitro and lung metastasis in vivo [21]. Yadav et al. revealed that silencing of ALKBH5 increases m^6A levels and consequently destabilizes USP22 and RNF40, resulting in reduced expression of several genes associated with cell cycle, replication and DNA damage repair in osteosarcoma cells. [22]. However, the role of histone methylation modification in the regulation of DNA repair leading to chemotherapy resistance in OS remains unclear, and histone methylation could be a potential therapeutic signaling for chemo-resistant OS patients.

In this study, we first identified histone methylation and related pathways in OS TME,comparing malignant proliferation cells with other cell subgroups by utilizing scRNA-seq data. We further investigating the potential therapeutic targets in methionine metabolism to reduce the level of histone methylation mollification, integrating compound screening, in vitro and in vivo biological expiration. We explored that combination of MAT2A and EZH2 inhibition could significantly reduce the intracellular H3K27me3 level and induce DNA damage. These findings might present a promising therapeutic strategy for chemotherapy-resistance OS.

2. Methods

Study cohort and collection of clinical human samples. Our study was approved by the Institutional Research Ethics Committee of Shanghai General Hospital, Shanghai Jiao Tong University School of Medicine. Samples of SGH-OS including in this study were collected in the core of the tumor resections. Pathological diagnoses of all the OS patients admitted in Shanghai General Hospital were independently examined by three pathologists. the Kaplan–Meier survival curves compared by two-side long-rank test was performed using R2 Genomics Analysis and Visualization Platform (R2, https://hgserver1.amc.nl/cgi-bin/r2/main.cgi).

Analysis of single-cell RNA sequencing (scRNA-seq). The single-cell RNA sequencing (scRNA-seq) data used in this study were derived from comprises previously published data (n = 16), including six individuals from Liu et al. (GSE162454) (https://www.ncbi.nlm.nih.gov/geo/query/acc.cgi?acc=GSE162454) and ten individuals from Zhou Y et al. (GSE152048) [23]. The raw data were processed using the Seurat package (v4.0, http://satijalab.org/seurat/) and analyzed in R software (v4.2.0). The Seurat object contained gene expression data for each sample and was imported using the Read 10 × function. We filtered out cells with fewer than 300 or more than 6000 detected genes, or with mitochondrial gene content exceeding 10 % of total expressed genes. Data normalization was performed using log normalization with the default scaling factor. Subsequently, the highly variable genes (HVGs) were identified from the normalized expression matrix, centered, and scaled before conducting principal component analysis (PCA). Single-cell data integration and analysis were performed using the canonical correlation analysis (CCA) method in Seurat. Clustering analysis was conducted based on the integrated joint embedding data, and the Uniform Manifold Approximation and Projection (UMAP) method was used for visualization. Specific cells from lung tissue were removed, resulting in a total of 99,416 filtered cells for further bioinformatics analysis. Cell cluster annotation was performed using the Wilcoxon rank-sum test in Seurat, with Bonferroni correction applied to identify differentially expressed genes (DEGs) with high discriminatory ability. Cell subpopulations were annotated based on these DEGs. The analysis of cell receptor–ligand interactions was conducted using the iTALK package in R (https://github.com/Coolgenome/iTALK) [24]. Given that osteosarcoma arises from the mesenchymal lineage, malignant tumor cells often resemble mesenchymal stromal cells (MSCs) in their transcriptomic profiles. Therefore, conventional tumor cell markers such as EpCAM are not applicable. In this study, we adopted a classification approach based on transcriptomic similarity and canonical lineage markers, which yielded mesenchymal, myeloid, lymphoid, and endothelial populations. This clustering strategy is consistent with previous osteosarcoma single-cell studies [25,26]. To distinguish malignant from non-malignant MSC subpopulations, we further examined proliferation signatures (*MKI67*, *PCNA*) and copy number variation (CNV) scores inferred by the inferCNV method.

Quality control steps in scRNA-seq analysis. Mitochondrial gene content (percent.mt): For each sample, we used the PercentageFeatureSet function to calculate the mitochondrial gene content using the mitochondrial gene pattern "^MT-". Cells with mitochondrial gene content exceeding 10 % were excluded, as this typically indicates that the cells are under stress or undergoing apoptosis.Gene count and mitochondrial proportion filtering: Cells were filtered based on the number of genes detected (200–10,000 genes) and mitochondrial gene content (below 10 %). This step helps ensure that only viable, non-apoptotic cells are retained for analysis.Red blood cell gene expression (percent.HB): We calculated the expression of red blood cell genes (e.g., HBA1, HBB) and excluded cells with more than 1 % red blood cell gene expression. This step removes cells that may be contaminated by red blood cells.Doublet detection and removal: Doublets were identified using the DoubletFinder package. The expected doublet proportion was set to 7.5 % (0.075 * number of cells), and principal component analysis (PCA) with 30 principal components was used to detect doublets. Cells predicted to be doublets were removed from the dataset.Data normalization and variable gene selection: Data were normalized using the NormalizeData function, followed by detection of variable genes using the FindVariableFeatures function. We then performed data scaling using ScaleData and conducted PCA analysis on the normalized data.

Cell lines, antibodies, and reagents. The human osteosarcoma cell lines HOS, HOS/MNNG, 143B, SJSA-1, ZOSM, ZOS2 and U2-OS, and the human kidney cell line HEK-293T were cultured in high glucose Dulbecco's Modified Eagle Medium (DMEM; Gibco, USA) supplemented with 10 % fetal bovine serum (FBS; Wisent, Canada). Cell line authentication was performed on cells that used for in vitro and in vivo studies using Short Tandem Repeat (STR) DNA profiling and all cell lines were

preserved at Shanghai Bone Tumor Institute (Shanghai, China). Cell lines are regularly tested for mycoplasma contamination. ZOSM and ZOS2 were obtained from the first affiliated hospital of Sun Yat-Sen University (Guangzhou, China). The human mesenchymal stem cell (HMSC) and adipose-derived stem cells (ADSC) was cultured in Dulbecco's Modified Eagle Medium/Nutrient Mixture F-12 (DMEM/F-12) medium (Gibco, USA) supplemented with 10 % fetal bovine serum (FBS; Wisent). All cell lines were cultured at 37 °C in a 5 % CO_2 incubator. Reagents used in the study included PF-9366 (#HY-107778, MedChemExpress, USA), SCR6639 [27] and GSK126 (#HY-13470, MedChemExpress, USA). The antibodies used in this study were purchased as follows: anti-GAPDH (#ab181602, 1:1000, Abcam, USA), anti-beta actin (#ab8226, 1:1000, Abcam, USA), and anti-EZH2 (#ab283270, 1:1000, Abcam, USA), anti-H3K27me3 (#MA5-11198, 1:1000 for western blotting and 3ug for ChIP-seq, Invitrogen, USA), anti-H3K27ac (#720096, 1:1000, Invitrogen, USA), anti-histone H3 (#PA5-16183, 1:1000, Invitrogen, USA), anti-H3K36me3 (#MA5-24687, 1:1000, Invitrogen, USA) and anti-H3K36me2 (#701767, 1:1000, Invitrogen, USA), anti-MAT2A (#HPA043028, 1:1000 for western blotting and 1:500 for immunohistochemistry, Sigma–Aldrich, USA), anti-γH2Ax (#9718, 1:1000 for western blotting and 1:200 for immunofluorescence, Cell Signaling Technology, USA), HRP-conjugated goat anti-rabbit IgG (#L3042, 1:5000, Signalway Antibody, USA) and goat anti-mouse IgG (#101, 1:5000, Signalway Antibody, USA).

Bulk RNA sequencing (RNA-seq). RNA purity of specimens was checked using the kaiaoK5500 Spectrophotometer (Kaiao, China). RNA integrity and concentration was assessed using the RNA Nano 6000 Assay Kit of the Bioanalyzer 2100 system (Agilent Technologies, USA). A total amount of 2ug RNA per sample was used as input material for the RNA sample preparations. Sequencing libraries were generated using NEBNext Ultra RNA Library Prep Kit for Illumina (NEB, USA) according to the manufacturer's protocol and index codes were added to attribute sequences to each sample. The clustering of the index-coded samples was performed on a cBot cluster generation system using HiSeq PE Cluster Kit v4-cBot-HS (Illumina, USA) according to the manufacturer's instructions. After cluster generation, the libraries were sequenced on DNBSEQ-T7 platform (BGI, China) in Wuhan Benagen Technology Co., Ltd. (Wuhan, China) and 150 bp paired-end reads were generated.

Bulk RNA-seq data analysis. The raw data were first processed with FastQC to filter out adapters and low-quality sequences. Pair-end reads were aligned to human GRCh38 genome or mouse mm10 genome using STAR (v2.7.6a) [28]. Reads with good mapping quality (MAPQ >30) that aligned to genomic exons were counted using featureCounts [29] (GRCh38 or mm10 Ensembl 93) to generate a table with counts for each gene. Differential gene expression analysis was performed using the R package DESeq2 [30] using the IfcShrink function. Genes with fold-change ≥2.00, probability ≥0.80 and false discovery rate P value (FDR) < 0.05 were considered significantly differentially expressed. The transform between human genome and mouse genome was performed using the R package BioMart [31,32]. Gene Ontology (GO; http://geneontology.org/) enrichment analyses for differentially expressed genes were performed using the R package clusterProfiler v3.8 [33]. Gene set enrichment analysis (GSEA; http://www.gsea-msigdb.org/gsea/) [34] was performed on list of genes ranked from high to low DESeq2 estimated fold-change using the GSEAPreRanked function with enrichment statistic classic, 1000 permutations and normalized P value < 0.05. Related gene sets were downloaded from Molecular Signatures Database (MSigDB, https://www.gsea-msigdb.org/gsea/msigdb/) [35,36].

Chromatin immunoprecipitation sequencing (ChIP-seq). Cells were first cross-linked with 1 % formaldehyde at room temperature for 10 min to stabilize protein-DNA interactions, followed by quenching with 125 mM glycine. After washing with cold PBS, cells were lysed in lysis buffer (50 mM Tris–HCl, pH 8.0, 10 mM EDTA, 1 % SDS) supplemented with protease inhibitors. The lysed cells were then subjected to sonication using an ultrasonic processor. The chromatin samples were diluted in immunoprecipitation buffer (16.7 mM Tris–HCl, pH 8.0, 1.2 mM EDTA, 1.1 % Triton X-100, 167 mM NaCl) and pre-cleared with Protein A/G magnetic beads for 1 h at 4 °C. Subsequently, anti-H3K27me3 antibody was added, and the samples were incubated overnight at 4 °C to complete the immunoprecipitation. Immunocomplexes were captured using Protein A/G magnetic beads and washed sequentially with low-salt wash buffer, high-salt wash buffer, LiCl wash buffer, and TE buffer to remove nonspecific bindings. Chromatin was eluted from the beads using elution buffer (1 % SDS, 0.1 M $NaHCO_3$) and subjected to reverse cross-linking at 65 °C overnight. Proteinase K was added, and the samples were digested at 55 °C for 2 h, followed by DNA purification. Sequencing libraries were constructed, and sequencing was performed using Illumina to generate 150 bp paired-end reads. Sequencing data were analyzed through a standard bioinformatics pipeline. Raw reads were trimmed using Trimmomatic (https://github.com/usadellab/Trimmomatic) to remove adapters and low-quality bases, and the cleaned reads were aligned to the human genome (GRCh38) using Bowtie2. Peaks were identified using MACS2 (v2.2.7) and annotated to the nearest genes using HOMER (homer.ucsd.edu/homer/). Binding regions were visualized using IGV(IGV: Integrative Genomics Viewer).

Compound screens. OS cells were screened with metabolite library (n = 540,list in Supplementary Table 1). Plant cells 800/well in 50ul medium into 384-well plates, transfer 0.1ul compound (1 mM) using pintool (final concentration 2 μM). Each plate included 32 wells containing DMSO as negative control. Incubate for 3 days, then add Celltiter Glo cell viability assay kit (#G7570, Promega, USA) 10ul/well to detect cell viability.

Western blotting. Proteins were extracted by using radio immunoprecipitation assay (RIPA) lysis buffer (Beyotime, China) for total protein and Histone Extraction Kit (#ab113476, Abcam, USA) for histone following its manufacturer's protocol. The extracted protein was quantified using a Pierce BCA Protein Quantification Kit (#23325, Thermo Fisher Scientific, USA) calculated using SpectraMax M3 Microplate Reader (Molecular Devices, USA). Proteins were separated by sodium dodecyl sulfate polyacrylamide gel electrophoresis (SDS-PAGE) and transferred to 0.45um polyvinylidene fluoride (Millipore, USA) using Mini-PROTEAN Tetra Vertical Electrophoresis Cell electrophoresis chamber and Mini Trans-Blot Module for tank transfer system with PowerPac HV Power Supply (Bio-Rad, USA). The membrane was blocked using 5 % nonfat dry milk in Tris-buffered saline solution containing 0.1 % Tween-20 (TBS-T) for 1h at room temperature and then probed with specific primary antibodies overnight at 4 °C. Subsequently, the membranes were washed with TBS-T 10 min for third times, followed by incubating with HRP-conjugated secondary antibodies for 1h at room temperature. Actin and GAPDH were used as the protein loading control. Protein signals were developed with SuperSignal West Femto Maximum Sensitivity Substrate (Thermo Fisher Scientific, USA) and imaged using chemiluminescence imaging system Amersham Imager 600 (GE Healthcare, USA) and Tanon 5200 (Tanon, China).

Cell viability assay and colony formation. To assay cell growth, osteosarcoma cells were washed twice with PBS and plated onto 60 mm cell culture dishes at a density of 3000 cells per dish. Osteosarcoma cells were treated with or without drugs for 1 week, and the cell colonies were stained using crystal violet staining solution (Beyotime, China) according to the manufacturer's instructions. To assay cell viability, osteosarcoma cells were plated onto 96-well plates at a density of 3000 cells per well. Osteosarcoma cells were treated with or without drugs for 3 days, and cell viabilities were then measured by using a Cell Counting Kit-8 (CCK-8; #CK04, Dojindo, Japan) detected using SpectraMax M3 Microplate Reader (Molecular Devices, USA).

Incucyte cell proliferation assay, cell viability assay and caspase-3/7 apoptosis assay. Indicated cell lines were seeded into 96-well plates at a density of 1000–2000 cells per well, depending on the growth rate and the design of the experiment. About 24 h later, the indicated compounds were added at the indicated concentrations. Cells were imaged every 4 h using the Incucyte ZOOM (Essen Bioscience).

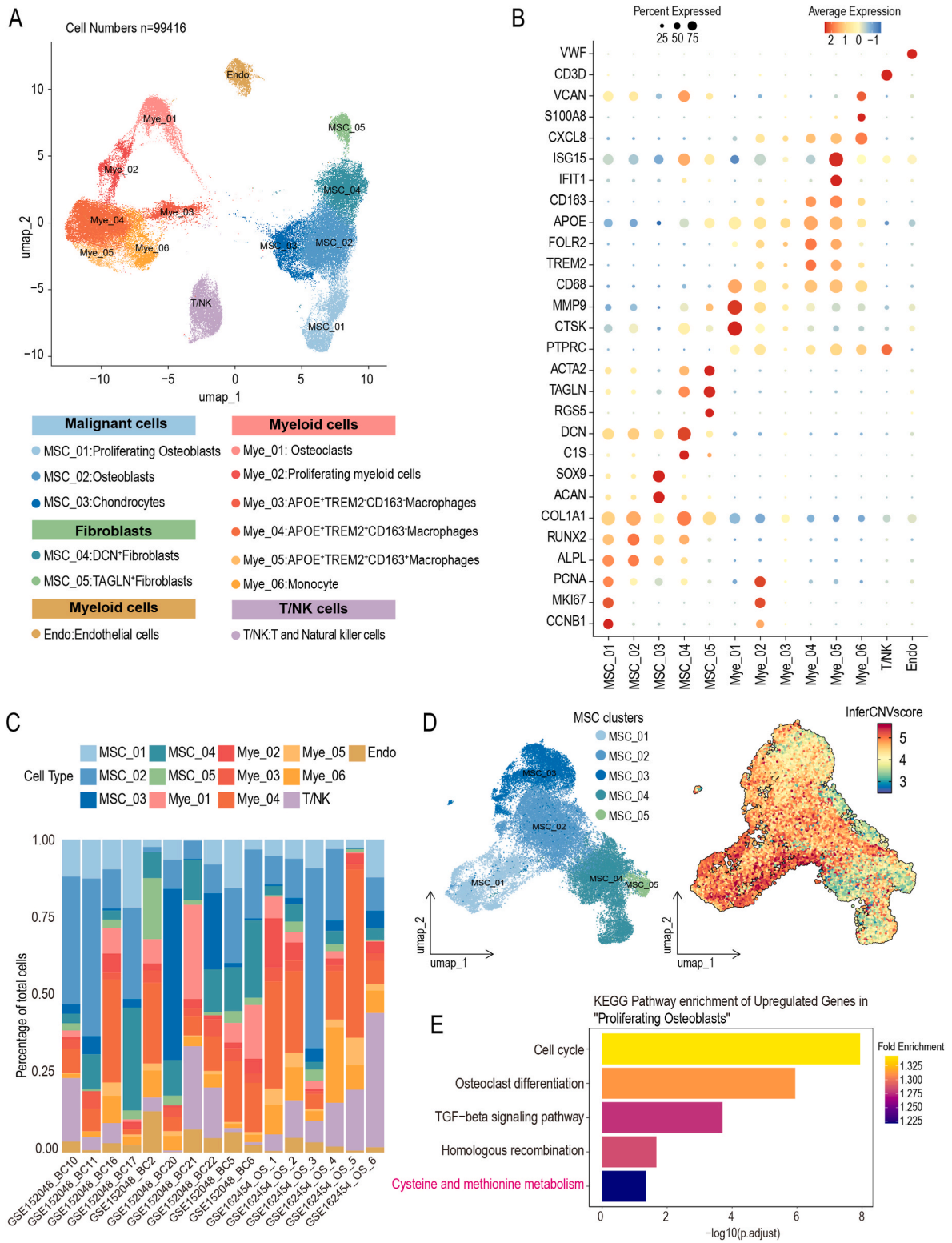

Fig. 1. Methionine metabolism pathway activation in tumor cells with malignant proliferation phenotype in the osteosarcoma microenvironment (A) UMAP visualization of single-cell transcriptomic data from osteosarcoma tumor samples, showing distinct cell clusters, including mesenchymal stem cells (MSC, MSC_01 to MSC_05), myeloid cells (Mye_01 to Mye_06), T cells and natural killer cells (T/NK), and endothelial cells (Endo). Cell numbers, n = 99416. (B) Stacked bar plot showing the proportion of different MSC, Mye, Lym and Endo subtypes (MSC_01 to MSC_05, Mye_01 to Mye_06, T/NK and Endo) across various single-cell datasets from osteosarcoma samples, demonstrating heterogeneity within the total cells populations. (C) Dot plot showing the percentage and average expression of marker genes for each cell type. (D) Chromosomal instability was assessed across mesenchymal-origin subpopulations using InferCNV. (E) Top 5 significantly enriched KEGG biological pathways in MSC_01 compared to (MSC_02, MSC_03, MSC_04 and MSC_05). Pathways include Cell cycle, Osteoclast differentiation, TGF-beta signaling pathway, Homologous recombination, and Cysteine and methionine metabolism.

Phase-contrast images were analyzed to detect cell proliferation on the basis of cell confluence. For cell viability assay, CellTiter-blue (Promega, G8081) was added to the medium following the manufacturer's instructions. For cell apoptosis, caspase-3/7 apoptosis-assay reagent was added to the culture medium, and cell apoptosis was analyzed on the basis of fluorescent staining of apoptotic cells.

EdU Incorporation Assay. Cell proliferation was assessed using the EdU (5-ethynyl-2′-deoxyuridine) incorporation assay with the Meilun EdU Cell Proliferation Kit with Alexa Fluor 555 (Cat. No. MA0425, Meilunbio, China) following the manufacturer's instructions. Briefly, osteosarcoma cells were seeded in 6-well plates and incubated overnight. EdU was added to the culture medium at a final concentration of 10 μM and cells were incubated for 2 h at 37 °C. After incubation, cells were fixed with 4 % paraformaldehyde for 30 min at room temperature, permeabilized with 0.3 % Triton X-100 in PBS, and subjected to Click-iT reaction with Alexa Fluor 555 Azide in the presence of $CuSO_4$ and Click-iT additives. Nuclei were counterstained with Hoechst 33342. EdU-positive cells were visualized under a fluorescence microscope and quantified using ImageJ software. Three biological replicates were performed for each condition.

Animal experiments. All animal experiments were performed by following the protocols in accordance with the guidelines of Laboratory Animal Center of Shanghai General Hospital. The Clinical Center Laboratory Animal Welfare & Ethics Committee of Shanghai General Hospital, Shanghai Jiao Tong University School of Medicine, approved all animal protocols used in this study. 6-8-week-old female Nude mice (Strain: BALB/cJGpt-foxn1nu/Gpt; Charlers river, USA/China) were used in this study. All mice were maintained under SPF conditions in a controlled environment of 20–22 °C, with a 12/12h light/dark cycle, 50–70 % humidity. The subcutaneous tumor-bearing mouse model was established by injecting OS cells (5×10^5 cells in 25ul PBS supplemented with 10 % FBS) into the lateral abdominal region of nude mice using a 27-gauge needle. OS progression in the mice was monitored by measuring the tumor volume, calculated by the following equation: Volume = Length × $\text{Width}^2/2$, using a caliper. The tumor burden was monitored by following the tumor volume and the maximal tumor size is 2 cm, which was permitted by the Clinical Center Laboratory Animal Welfare & Ethics Committee of Shanghai General Hospital, Shanghai Jiao Tong University School of Medicine. The maximal tumor size was confirmed to be not exceeded in our study and the survival curves were produced according to the survival of mice and the time to reach maximum tumor size. Samples was from the core of tumor resections. For methionine diet restriction studies, the mice were evaluated by monitoring tumor volume to quantify OS burden before for randomization and in the progress of drug treatment for efficacy evaluation. 14 days prior to constructing the tibia orthotopic model of osteosarcoma in mice, the methionine restriction group was placed on a methionine-restricted diet (containing 0.12 % methionine), while non-restriction group received a normal diet (containing 0.86 % methionine) [37].

Immunofluorescence staining and imaging. Cells on the glass bottom culture dishes (#801001, NEST, China) were fixed in 4 % parafomaldehyde (diluted the 32 % paraformaldehyde in PBS) for 10 min at room temperature. Cells were washed three times for 5 min with 200 mM glycine containing PBS, followed by permeabilization with 0.3 % Triton X-100 in PBS for 15 min. After blocking with 5 % bovine serum albumin (BSA) in PBS for 1 h, cells were incubated with mentioned primary antibody (γH2Ax) diluted in a 5 % BSA in PBS solution overnight at 4 °C. After washing four times with PBS, cells were incubated with Alexa Fluor Plus 555 (1:500; #A32732, Invitrogen, USA) secondary antibody for 1 h at room temperature and washed three times with PBS. Cell nuclei were then counterstained with DAPI (Beyotime, China) for 5 min. Cells were washed two more times in PBS before imagine. Images were acquired using Leica TCS SP8 Laser Scanning Confocal Microscope (Leica, USA) and were processed by Leica Application Suite X (LAS X; Leica, USA).

Stable gene overexpression and shRNA Knock-Down constructs. EZH2 overexpression using plasmid (5′- GCGAATTCGAAGTA-TACCTCGAGGCCA -3′), constitutive expression of shRNA hairpins targeting MAT2A (KD1: 5′- AGCAGTTGTGCCTGCGAAATA -3′, KD2: 5′-GCAACAGTCACCAGATATTGC -3′)or a scramble non-targeting control (5′-TTCTCCGAACGTGTCACGT-3′) was achieved using lentiviral infection of the pGMLV vector (modified from Genomeditech, Shanghai, China), selected with puromycin (2ug/ml). Constitutive overexpression of MAT2A in HOS/MNNG cell line was achieved using lentiviral infection of pGMLV vector (modified from Genomeditech, dual Promoter EF1-ZsGreen1-T2A-Puro), selected with puromycin (2ug/ml).

Lentivirus generation and harvesting. Lentivirus production was obtained from PEI transfection reagents (#26406, Polysciences, USA) of HEK-293T cells with co-transfection of the packaging vectors pspax2 and pMD2.G along with the gene delivery vector. Viral supernatants were collected 72h after transfection, underwent ultracentrifugation at 20,000 rpm for 25h at 4 °C to concentrate, and the virus pellets were resuspended in PBS. For infection, the viral pellets were added to cells in a dropwise manner in the presence of polybrene (10ug/ml). After 48h, medium containing the lentivirus was replaced and infected cells were selected by addition of puromycin (2ug/ml).

Statistical analysis. Details of statistical analyses of the various experiments are described in the relevant methods section. If not specified, statistical analysis was carried out using GraphPad Prism 8 software (GraphPad Software, USA). After confirming that values followed a normal distribution, two-tailed Student's t test was applied to determine the significance of differences between two groups of independent samples. Pearson's correlation analysis and Spearman's correlation analysis were performed to determine the correlation between two group of variables. Combination index (CI) of drug combination was calculated using ComboSyn software program (ComboSyn, USA) to determine whether the combination was antagonistic, additive or synergistic. The image was subjected to gray value analysis using ImageJ software (Thermo Fisher Scientific, USA). Details of the data points shown were described in the respective figure legends. All schematic diagrams were created using BioRender (BioRender.com).

3. Results

3.1. Methionine metabolism pathway activation in tumor cells with malignant proliferation phenotype in the osteosarcoma microenvironment

To investigate the microenvironmental features of OS and the molecular pathways associated with malignant proliferation, we analyzed single-cell transcriptomic data from tumor samples (n = 99,416 cells). The data was partitioned into 13 cellular subgroups, including 5 mesenchymal-origin subgroups (MSC_01 to MSC_05),6 myeloid-lineage subgroups (Mye_01 to Mye_6), 1 lymphoid-lineage subgroups (Lym), and 1 endothelial subgroup (Endo) (Fig. 1A), including: (1) MSC_01, proliferating osteoblastshighly expressing MKI67 and PCNA; (2) MSC_02, osteoblasts highly expressing RUNX2, COL1A1, and ALPL; (3) MSC_03, chondrocytes highly expressing ACAN and SOX9; (4) MSC_04, fibroblasts highly expressing DCN; (5) MSC_05, fibroblasts highly expressing TAGLN; (6) Mye_01, osteoclasts; (7) Mye_02, proliferating myeloid cells; (8) Mye_03, Macrophages highly expressing APOE and poorly expressing TREM2, CD163; (9) Mye_04, Macrophages highly expressing APOE and TREM2 and poorly expressing CD163; (10) Mye_05, Macrophages highly expressing APOE, TREM2 and CD163; (11) Mye_06, Monocytes; (12) T/NK, T cells and natural killer cells highly expressing of CD3D and PTPRC; (13) Endo, endothelial cells highly expressing of VWF (Fig. 1B). The proportions of these cell subpopulations varied significantly among different patient samples (Fig. 1C), highlighting the high heterogeneity of OS. InferCNV analysis showed that MSC_01 had the highest chromosomal instability scores among all 5 mesenchymal-origin subgroups (Fig. 1D), a hallmark of malignancy. In addition, MSC_01 was enriched for osteogenic and chondrogenic gene expression, consistent with the molecular

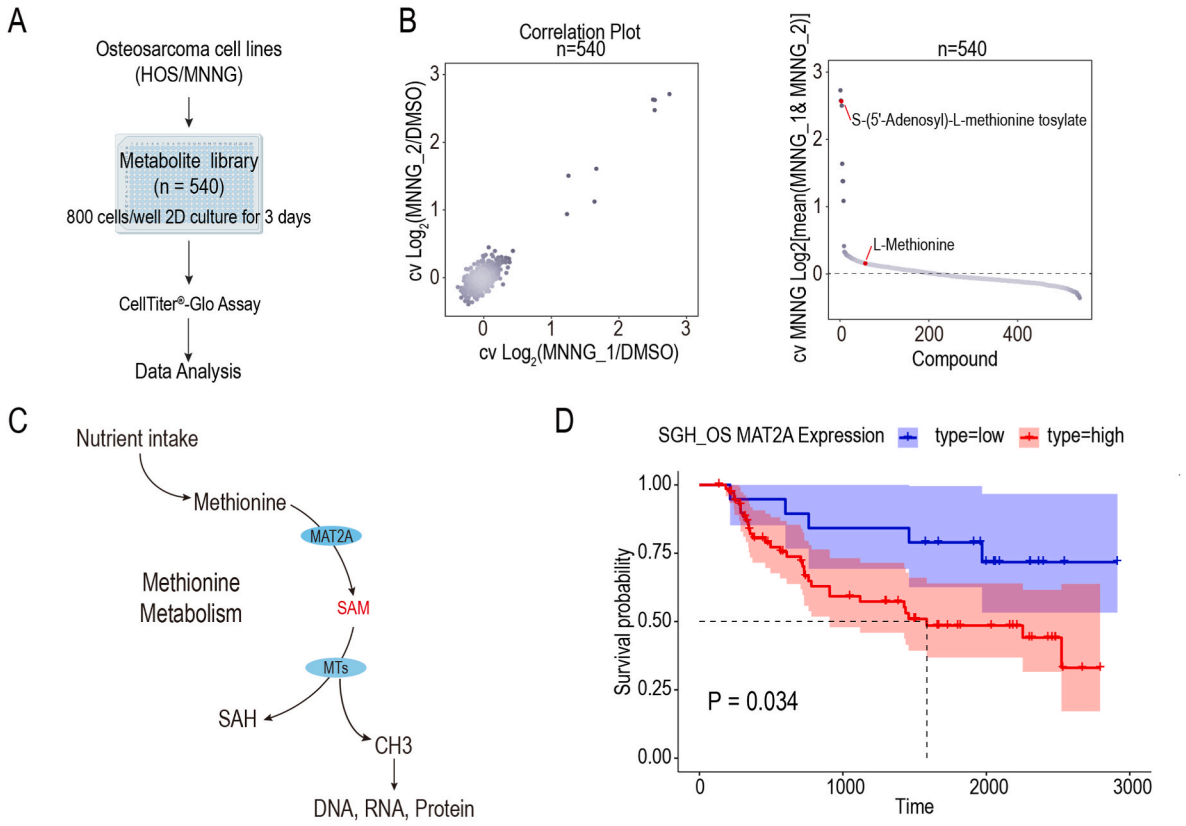

Fig. 2. High-throughput screening identifies methionine-metabolism is important in osteosarcoma tumor growth. (A) Schematic of the high-throughput screening workflow using the human osteosarcoma cell line HOS/MNNG. A library of 540 metabolites was screened in 2D cell culture (800 cells/well) for 3 days, followed by CellTiter-Glo® assay to assess cell viability. (B) Correlation plots of metabolite effects on cell viability. Left: Scatterplot of replicate data showing high consistency (n = 540 metabolites). Right: Highlighted metabolites (S-(5′-Adenosyl)-L-methionine tosylate and L-Methionine) significantly enhance cell viability compared to the DMSO control. (C) Schematic of the methionine cycle. Methionine is converted to S-adenosylmethionine (SAM) by MAT2A, serving as a methyl donor for DNA, RNA, and protein methylation. (D) Kaplan–Meier survival curve of osteosarcoma patients stratified by SGH_OS MAT2A expression. Patients with high MAT2A expression (n = 72) exhibit significantly poorer survival compared to those with low MAT2A expression (n = 19) (p-value = 0.034). Shaded areas represent 95 % confidence intervals, and the number of patients at risk is indicated below the graph.

characteristics of osteosarcoma tumor cells. Given its pronounced malignant features, including elevated CNV scores and high expression of proliferation markers (MKI67, PCNA), MSC_01 was identified as the primary malignant tumor cell population. We compared the MSC_01, with other cell mesenchymal-origin subgroups (MSC_02, MSC_03, MSC_04 and MSC_05) in the TME. We found that the Cysteine and methionine metabolism were upregulated in MSC_01. Additionally, Cell cycle, Osteoclast differentiation, TGF-beta signaling pathway and Homologous recombination pathways were also significantly upregulated (Fig. 1E). This suggests that in the osteosarcoma microenvironment, malignant proliferating tumor cells exhibit upregulation of the methionine metabolism pathway.

3.2. *High-throughput screening identifies methionine-metabolism is important in osteosarcoma tumor growth*

To investigate the impact of metabolites on the malignant proliferation and viability of osteosarcoma cells, we conducted high-throughput screening using a library of 540 metabolites on the human osteosarcoma cell line HOS/MNNG and 143B (Fig. 2A). Cells were treated with metabolites from the library, and cell viability was assessed after 3 days. The results showed significant variability in the effects of different metabolites on HOS/MNNG and 143B cell viability. We identified metabolites that significantly enhanced cell viability (Fig. 2B,Supplementary Fig. 1D and Supplementary Table 1), including L-Methionine, suggesting that methionine metabolism may play a crucial role in the malignant proliferation of osteosarcoma cells. AdoMet tosylate enhanced the viability of HOS/MNNG cells, whereas it had minimal effect on 143B cells. This observation further highlights the metabolic heterogeneity among osteosarcoma cell lines. AdoMet tosylate (S-Adenosylmethionine p-toluenesulfonate, SAM Tosylate) is a salt form of S-Adenosylmethionine (SAM).

SAM is a critical biomolecule that serves as a methyl donor or cofactor in various biological processes [38,39]. The conversion of methionine to SAM, a key methyl donor [40], requires the enzyme methionine adenosyltransferase (MAT2A) (Fig. 2C). To determine whether MAT2A is associated with osteosarcoma prognosis, we performed Kaplan–Meier survival analysis using the clinical database SGH-OS established from our previous multi-omics studies. The results indicated that patients with high MAT2A expression (n = 72) had significantly shorter survival times compared to those with low MAT2A expression (n = 19) (Fig. 2D). Single-cell transcriptomic analysis revealed that MAT2A is broadly expressed across cell types, with the highest levels observed in a subset of myeloid cells (Supplementary Fig. 1A). However, among mesenchymal stromal cells, MSC_01 showed the highest MAT2A expression. Importantly, MSC_01 was the only population exhibiting significant enrichment of cysteine and methionine metabolism and histone methylation pathways (Supplementary Fig. 1B–C). These results suggest that MAT2A plays a pivotal role in methionine-dependent epigenetic remodeling in osteosarcoma, supporting its functional importance and prognostic relevance in the tumor microenvironment.

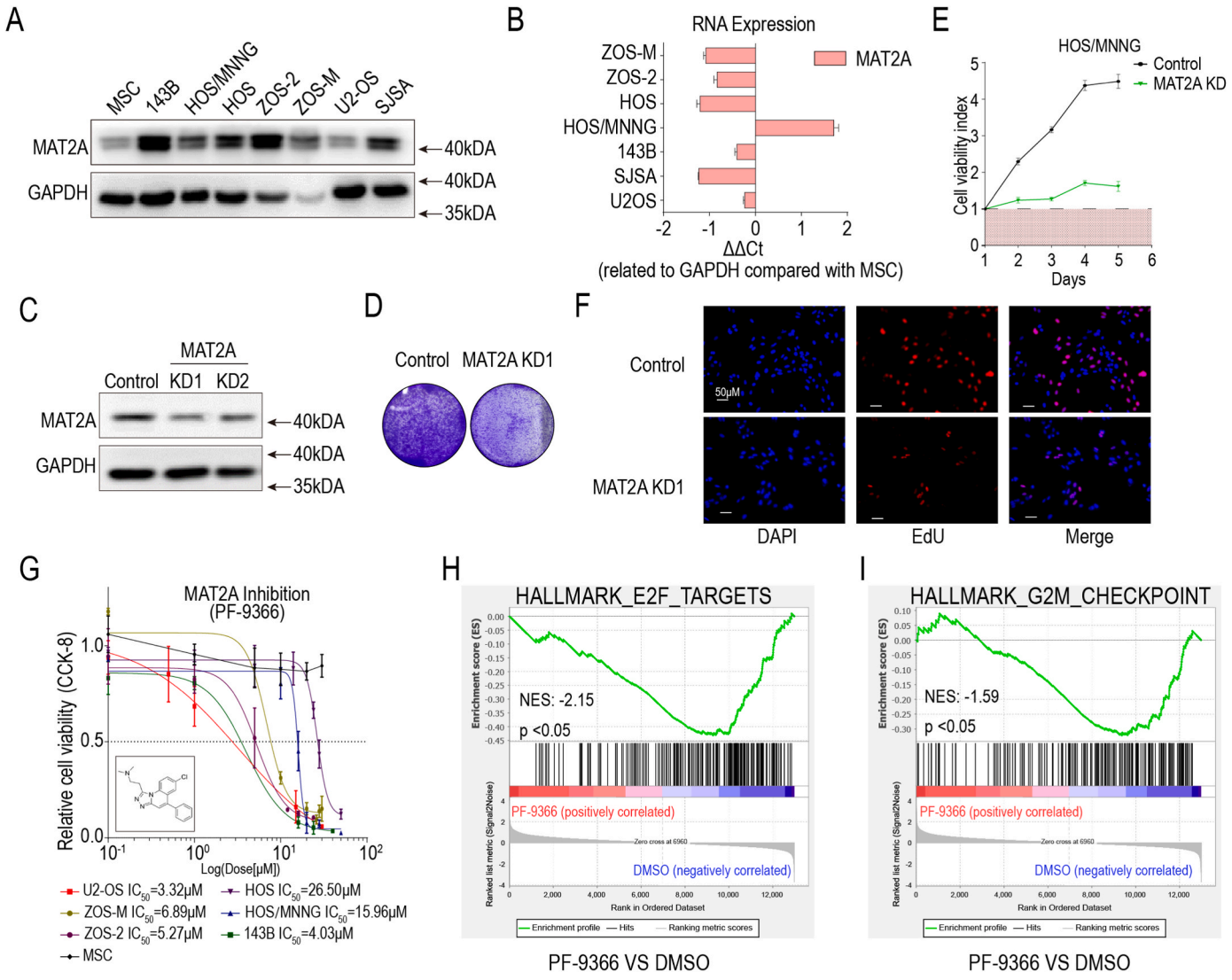

Fig. 3. Inhibiting MAT2A suppresses osteosarcoma cell proliferation and growth via cell cycle and DNA damage pathways (A) Western blot analysis of MAT2A protein levels in human osteosarcoma cell lines (143B, HOS/MNNG, HOS, ZOS-2, ZOS-M, U2-OS, SJSA) and human mesenchymal stem cells (HMSC). (B) RT-PCR analysis of MAT2A mRNA levels in the same osteosarcoma cell lines and MSC. (C) Construction of MAT2A knockdown cell models in HOS/MNNG cells, validated by western blot. (D) Colony formation assay to evaluate proliferation in MAT2A knockdown models. (E) CCK8 assay to measure cell viability in MAT2A knockdown models. Technical replicates = 5, Mean ± SD. (F) EdU incorporation assays were performed to assess the effect of MAT2A knockdown on cell proliferation. Scale bar: 50 μm. (G) CCK8 assay determining the IC50 values of PF-9366 in osteosarcoma cell lines and MSC. Technical replicates = 5, Mean ± SD. (H–I) Gene Set Enrichment Analysis (GSEA) of RNA-seq data comparing PF-9366-treated cells to DMSO controls. Downregulated pathways include HALLMARK_E2F_TARGETS (NES = −2.15, p-value <0.05) and HALLMARK_G2M_CHECKPOINT (NES = −1.59, p-value <0.05), indicating suppression of cell cycle-related processes. NES: Normalized Enrichment Score.

3.3. Inhibiting MAT2A suppresses osteosarcoma cell proliferation and growth via cell cycle and DNA damage pathways

To further investigate the role of MAT2A in osteosarcoma (OS), we assessed MAT2A protein and mRNA expression levels in human OS cell lines (143B, HOS/MNNG, HOS, ZOS-2, ZOS-M, U2-OS, SJSA) and human mesenchymal stem cell line (HMSC) (Fig. 3A and B). While metabolite screening was initially performed using the HOS/MNNG cell line to ensure data consistency and avoid batch effects, the subsequent expression and functional analyses across a broader panel of OS cell lines provided validation of the observed findings and supported the generalizability of MAT2A-related effects in OS. The results showed significantly higher MAT2A protein expression in OS cell lines compared to MSC. At the mRNA level, HOS/MNNG exhibited markedly higher MAT2A expression than other OS cell lines. Next, we constructed MAT2A knockdown (MAT2A KD) models in the HOS/MNNG cell line using shRNA and verified the models using Western blot (Fig. 3C). Colony formation assays showed a significant decrease in proliferation in MAT2A KD cells (Fig. 3D). CCK-8 assays revealed that MAT2A KD significantly reduced cell viability (Fig. 3E). To further validate the anti-proliferative effect of MAT2A inhibition, we performed EdU incorporation assays. MAT2A knockdown markedly reduced the proportion of EdU-positive cells compared to the control group (Fig. 3F). These results suggest that MAT2A protein expression affects OS growth. To further confirm the effect of MAT2A on OS proliferation, we treated OS cell lines and HMSC with the MAT2A inhibitor PF-9366 [41] and measured IC_{50} values using CCK assays. The IC_{50} values of the six osteosarcoma cell lines U2-OS, ZOS-M, ZOS-2, HOS, HOS/MNNG and 143B were 3.32 μM, 6.89 μM, 5.27 μM, 26.50 μM, 15.96 μM, and 4.03 μM, respectively (Fig. 3F). Interestingly, the three homologous cell lines (143B, HOS/MNNG, and HOS) share the same genome; however, their IC_{50} values under PF-9366 treatment exhibited significant differences. The

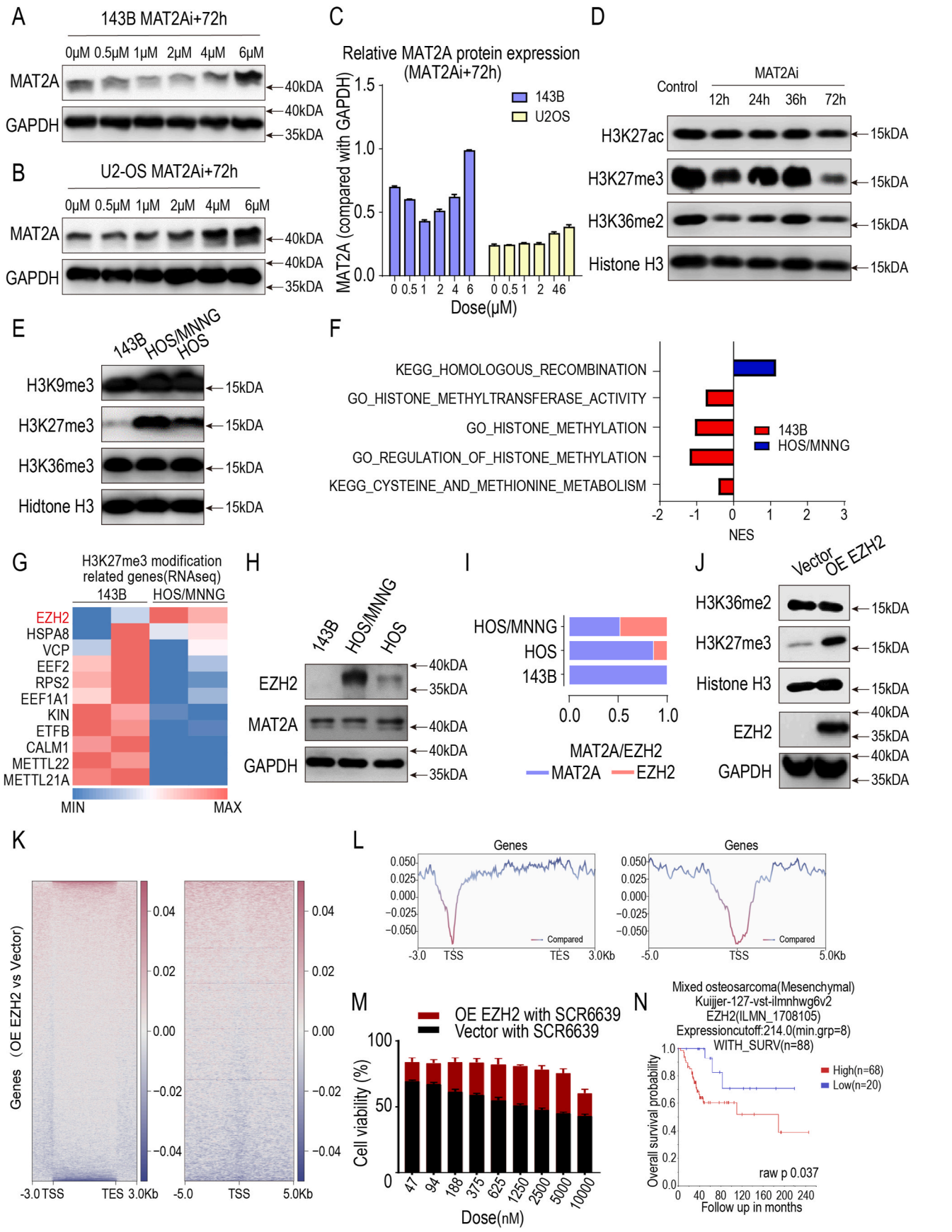

(caption on next page)

Fig. 4. MAT2A inhibition affects tumor growth *ex vivo* through EZH2-mediated H3K27me3 modification. (A) Western blot analysis of MAT2A protein levels in 143B cells treated with PF-9366 at different concentrations (0.5 μM, 1 μM, 2 μM, 4 μM, 6 μM) for 72 h. (B) Western blot analysis of MAT2A protein levels in U2-OS cells treated with PF-9366 at different concentrations (0.5 μM, 1 μM, 2 μM, 4 μM, 6 μM) for 72 h (C) RT-PCR analysis of MAT2A mRNA levels in 143B and U2-OS cells treated with PF-9366 at varying concentrations for 72 h. Technical replicates = 3, Mean ± SD. (D) Western blot analysis of epigenetic marks (H3K27ac, H3K27me3, and H3K36me2) in HOS/MNNG cells treated with MAT2A inhibitor (MAT2Ai) for 12, 24, 36, and 72 h. (E) Western blot analysis of H3K27me3, H3K9me3, and H3K36me3 levels in osteosarcoma cell lines (143B, HOS/MNNG, and HOS). (F) Gene Set Enrichment Analysis (GSEA) results showing pathway enrichment differences between MAT2A-related genes in 143B and HOS/MNNG cells. (G) Heatmap of RNA-seq data showing differential expression of H3K27me3-related genes, including EZH2, in 143B and HOS/MNNG cells. (H) Western blot analysis of EZH2 and MAT2A protein levels in osteosarcoma cell lines. (I) Quantitative analysis of the relative MAT2A/EZH2 protein expression ratio. (J) Changes in H3K27me3 and H3K36me2 levels in HOS/MNNG cells after EZH2 overexpression (OE EZH2). (K–L) ChIP-seq analysis of EZH2 overexpression on H3K27me3 chromatin modifications. (K) Heatmap showing signal intensity changes in gene regions (−3 kb to +3 kb and −5 kb to +5 kb). (L) Line plot showing average signal distribution near transcription start sites (TSS) and transcription end sites (TES). (M) CCK8 assay evaluating the sensitivity of EZH2-overexpressing (OE EZH2) and control (Vector) cells to MAT2A inhibitor (SCR6639) at various doses. Technical replicates = 3, Mean ± SD. (N) Kaplan–Meier survival analysis based on EZH2 expression levels in osteosarcoma patients from the Kuijjer dataset (n = 88), performed using the R2 platform. Raw p = 0.037.

IC_{50} value was the lowest in 143B cells, followed by HOS/MNNG cells, and the highest in HOS cells. To explore the pathway-specific effects of PF-9366 on OS, we performed bulk RNA-seq analysis on OS cells treated with PF-9366. The results revealed significant downregulation of cell cycle-related pathways and upregulation of DNA damage-related pathways, including HALLMARK_E2F_TARGETS, HALLMARK_G2M_CHECKPOINT, GOBP_REGULATION_OF_INTRINSIC_APOPTOTIC_SIGNALING_PATHWAY_IN_RESPONSE_TO_DNA_DAMAGE, GOBP_POSTREPLICATION_REPAIR, GOBP_DOUBLE_STRAND_BREAK_REPAIR_VIA_SINGLE_STRAND_ANNEALING, GOBP_DNA_STRAND_ELONGATION_INVOLVED_IN_DNA_REPLICATION, GOBP_DOUBLE_STRAND_BREAK_REPAIR_VIA_BREAK_INDUCED_REPLICATION (Supplementary Fig. 2A–C,Fig. 3G and H). These results indicate that inhibiting MAT2A effectively suppresses OS cell proliferation and growth by cell cycle and DNA damage pathways.

3.4. MAT2A inhibition affects tumor growth ex vivo through EZH2-mediated H3K27me3 modification

Given the differential sensitivity of PF-9366 across various OS cell lines, we selected the two cell lines with the lowest IC_{50} values, U2OS and 143B, as models to investigate the effects of PF-9366. To further explore the effects of the MAT2A inhibitor PF-9366 on OS, we treated OS cell lines 143B and U2-OS with PF-9366 at concentration gradient (0.5 μM, 1 μM, 2 μM, 4 μM, 6 μM) for 72 h and measured MAT2A protein and mRNA levels. The results showed a dose-dependent increase in MAT2A expression at both the protein and mRNA levels (Fig. 4A–4C). These findings are consistent with previous studies reporting that PF-9366 functions as an allosteric inhibitor of MAT2A without reducing its expression levels, but rather suppresses enzymatic activity and downstream SAM production [41]. Considering the significant differences in sensitivity to PF-9366 among the homologous cell lines 143B, HOS/MNNG, and HOS, as well as the impact of PF-9366 on OS cell cycle-related pathways and DNA damage-related pathways, we next examined the effects of PF-9366 on histone modifications at different time points (12h, 24h, 36h, 72h). After 72 h of PF-9366 treatment, H3K27me3 levels were significantly reduced, while H3K27ac and H3K36me2 levels showed minimal changes (Fig. 4D). To investigate the reasons for the differences in sensitivity to PF-9366 among the three cell lines (143B, HOS/MNNG, and HOS), we assessed the histone modification levels in these cell lines. The results showed significant differences in H3K27me3 levels among the three cell lines, with 143B exhibiting the lowest levels, HOS showing intermediate levels, and HOS/MNNG displaying the highest levels. In contrast, H3K9me3 and H3K36me3 levels showed no significant differences (Fig. 4E). This suggests that the sensitivity of OS to PF-9366 may be associated with H3K27me3 levels, where lower H3K27me3 levels correspond to higher sensitivity to PF-9366. We compared the relevant pathways between HOS/MNNG and 143B. In 143B, pathways related to histone methylation and methionine metabolism were downregulated, while homologous recombination were upregulated in HOS/MNNG (Fig. 4F). This validated our hypothesis that OS sensitivity to PF-9366 is associated with histone modifications and methionine metabolism. Next, we analyzed the reasons for the differences in H3K27me3 levels in OS. We compared genes related to H3K27me3 between HOS/MNNG and 143B. The results showed that only EZH2 was expressed at lower levels in 143B while being highly expressed in HOS/MNNG (Fig. 4G). This suggests that the expression of EZH2 may be a key factor contributing to the differences in H3K27me3 levels in OS. We then validated the expression of EZH2 across the three OS cell lines. While MAT2A expression showed no significant differences among the three cell lines, EZH2 expression correlated with H3K27me3 levels, with the highest expression in HOS/MNNG and the lowest in 143B. We analyzed the protein expression ratio of MAT2A to EZH2 and found that the ratio was 1:1 in HOS/MNNG, differed in HOS and 143B (Fig. 4I). This suggests that maintaining high H3K27me3 levels requires a specific balance between MAT2A and EZH2 protein expression. To further confirm that the sensitivity of 143B cells to PF-9366 is due to the low expression of EZH2 leading to reduced H3K27me3 levels, we overexpressed EZH2 in 143B cells and observed an increase in H3K27me3 levels (Fig. 4J). ChIP-seq analysis showed that EZH2 overexpression significantly affected gene expression at transcription start sites (TSS) and transcription end sites (TES), with a more pronounced effect at TSS, consistent with the transcription-repressive nature of H3K27me3 (Fig. 4K and L). Treatment of EZH2-overexpressing 143B cells with a MAT2A inhibitor SCR6639 [27] revealed reduced sensitivity to MAT2A inhibition (Fig. 4M). To assess the prognostic value of EZH2 expression in clinical OS samples, we analyzed the Kuijjer dataset (n = 88) using the R2 platform. Kaplan–Meier analysis revealed that patients with high EZH2 expression had significantly poorer overall survival than those with low expression (Fig. 4N), suggesting potential clinical relevance of EZH2 as a prognostic marker in osteosarcoma. These experimental results indicate that MAT2A inhibition affects tumor growth *ex vivo* through EZH2-mediated H3K27me3 modification.

3.5. The synergistic effect of EZH2 and MAT2A inhibitors enhances DNA damage in osteosarcoma cells

Based on the above findings, the reason why HOS/MNNG and HOS are less sensitive to MAT2A inhibitors compared to 143B is the high level of H3K27me3 mediated by EZH2. This led us to investigate whether targeting H3K27me3 would affect OS growth. To address this, we performed a compound screening assay on OS cell lines (ZOS-M, ZOS-2, 143B, and HOS/MNNG), as well as HMSC and adipose-derived stem cells (ADSC). The compound library (n = 44) primarily targeted histone modifications, including PRMTs, H4K20, H3K79, H3K4, H3K36, and H3K27. The results showed that drugs targeting H3K27 exhibited high cytotoxic effects on osteosarcoma cells, particularly 143B and HOS/MNNG, while causing relatively low cytotoxicity to normal human cells (Supplementary Fig. 2D,Supplementary Table 2). Among the H3K27-targeting compounds, the EZH2 inhibitor GSK126 demonstrated particularly potent killing effects on 143B and HOS/MNNG cells, with

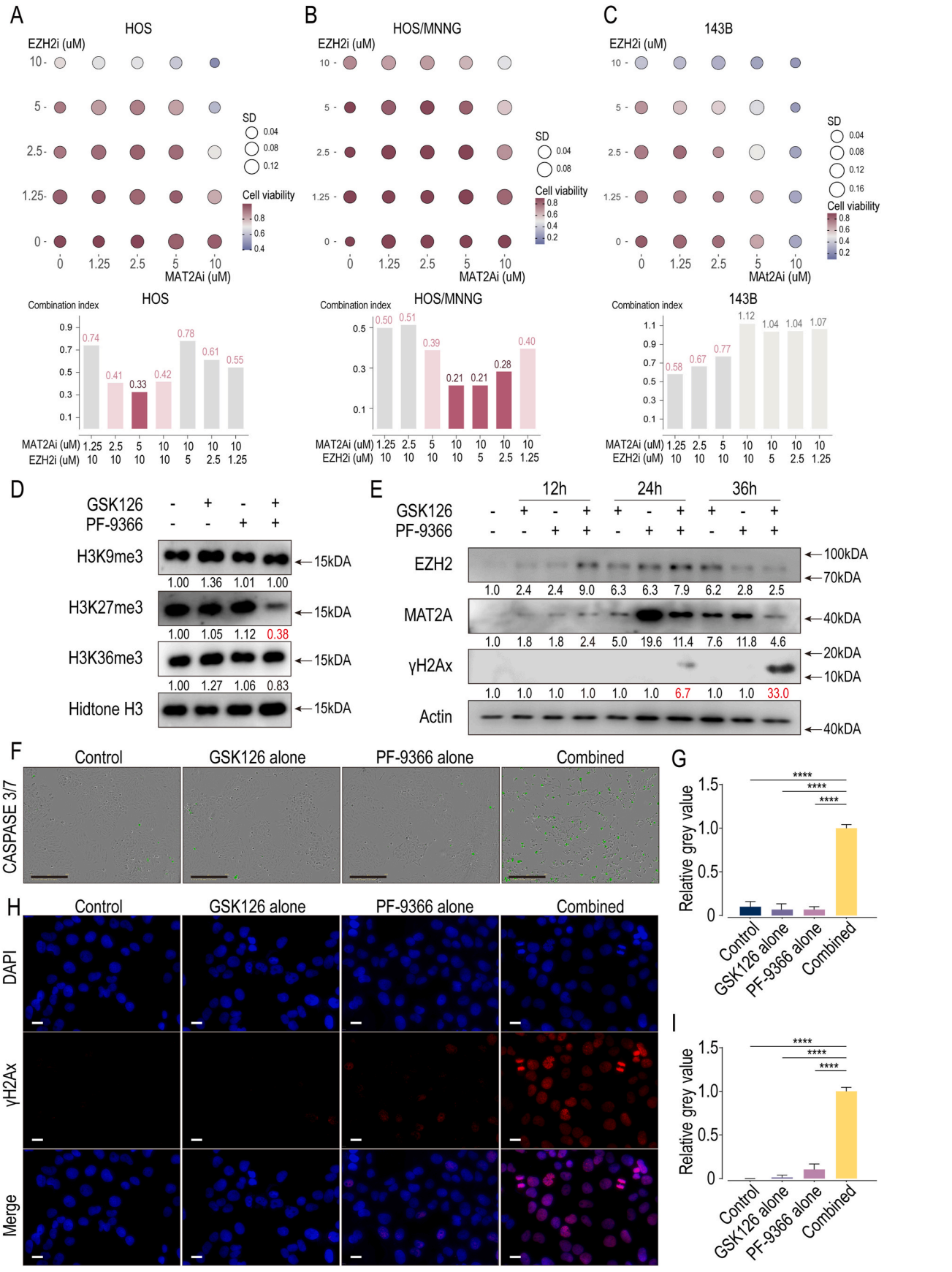

(caption on next page)

Fig. 5. The synergistic effect of EZH2 and MAT2A inhibitors enhances DNA damage in osteosarcoma cells. (A–C) Effects of EZH2 inhibitor (EZH2i, GSK126) and MAT2A inhibitor (MAT2Ai, PF-9366) on cell viability in osteosarcoma cell lines (HOS, HOS/MNNG, 143B). Upper panels: heatmap of cell viability; lower panels: combination index (CI) analysis. CI < 0.7 indicates synergy, and CI < 0.3 indicates strong synergy. (D) Western blot analysis of histone modifications (H3K9me3, H3K27me3, H3K36me3) after combined treatment with GSK126 and PF-9366. Technical replicates = 3. (E) Time-dependent changes in EZH2, MAT2A, and γH2AX levels in HOS/MNNG cells treated with GSK126 and PF-9366 for 12, 24, and 36 h. Technical replicates = 3. (F) CASPASE3/7 staining analyzed by Incucyte live-cell imaging after drug treatments. Scale bar: 400 μm. (G) Quantification of CASPASE3/7 fluorescence intensity after drug treatments, ****: $p < 0.0001$, Technical replicates = 3, Mean ± SD. (H) Immunofluorescence staining of DAPI and γH2AX in osteosarcoma cells treated with different drugs. Scale bar: 20 μm. (I) Quantification of γH2AX fluorescence intensity, ****: $p < 0.0001$, Technical replicates = 3, Mean ± SD.

minimal toxicity to normal human cells. We further investigated whether the simultaneous targeting of MAT2A and EZH2 would influence OS growth. We treated OS cell lines 143B, HOS/MNNG and HOS with a combination of the MAT2A inhibitor PF-9366 and the EZH2 inhibitor GSK126. The results showed that in 143B cells, which have low H3K27me3 levels, cell viability decreased progressively with increasing concentrations of the MAT2A inhibitor. In contrast, in HOS/MNNG and HOS cells, which have high H3K27me3 levels, MAT2A and EZH2 inhibitors exhibited a synergistic effect. Notably, HOS/MNNG cells, with a MAT2A/EZH2 protein expression ratio of 1:1, showed a particularly strong synergistic response (Fig. 5A–5C). Similarly, we further examined whether the combination of MAT2A and EZH2 inhibitors affected histone methylation in OS cells. The results showed that only the combined treatment led to a significant reduction in H3K27me3 levels, while H3K9me3 and H3K36me3 remained largely unaffected (Fig. 5D). We observed an increase in γH2Ax levels at 24 h following the combined treatment, with a more pronounced elevation at 36 h (Fig. 5E). CASPASE3/7 and γH2AX fluorescence signals were markedly enhanced in HOS/MNNG cells following combined treatment, indicating increased DNA damage and apoptosis (Fig. 5F–I). To validate these findings in an independent OS model, we performed the same assays in HOS cells. Consistently, we observed significantly elevated Caspase-3/7 activation and γH2AX expression in the combination group compared to single-agent treatments (Supplementary Fig. 3A–3D). These results confirm that the synergistic effect of MAT2A and EZH2 inhibition is reproducible across multiple osteosarcoma cell lines.

To evaluate whether this EZH2–H3K27me3 axis also shows heterogeneity in clinical osteosarcoma samples, we performed additional analyses using single-cell RNA-seq data from primary tumor samples. We examined the association between EZH2 expression and the module scores of the BENPORATH_ES_WITH_H3K27ME3 gene set, which represents PRC2/H3K27me3 target gene repression. Malignant cells were stratified into EZH2-high and EZH2-low groups based on median expression levels. We observed that EZH2-high cells exhibited significantly lower module scores (Wilcoxon rank-sum test, $p < 0.0001$), consistent with stronger H3K27me3-mediated transcriptional repression (Supplementary Fig. 3E). These results support the presence of functional heterogeneity in the EZH2–H3K27me3 pathway in clinical tumor settings, thereby reinforcing the biological rationale for the differential MAT2A inhibitor sensitivity observed in vitro. These experimental results suggest that the combination of EZH2 and MAT2A inhibitors significantly enhances DNA damage by reducing H3K27me3 levels, ultimately affects OS growth.

3.6. The synergistic effect of EZH2 inhibitor and methionine-restricted diet suppresses osteosarcoma growth in vivo

We conducted animal experiments to validate the therapeutic effects of targeting EZH2 and MAT2A, using GSK126 to inhibit EZH2 and implementing a methionine-restricted diet (MRD) as an alternative strategy for targeting MAT2A. The results demonstrated that both GSK126 and MRD alone suppressed tumor growth, while their combined treatment resulted in even more pronounced tumor growth inhibition (Fig. 6A and B). Moreover, mouse body weight remained stable across all treatment groups, indicating a high level of treatment safety (Fig. 6C). Immunohistochemical analysis revealed that both GSK126 and MRD reduced the expression levels of the proliferation marker Ki67 and H3K27me3 in tumor tissues. Notably, the combined treatment group showed a more significant decrease in Ki67 and H3K27me3 levels (Fig. 6D and E). Concurrently, the expression of the DNA damage marker γH2Ax was significantly increased in the combined treatment group, suggesting that EZH2 inhibition and MRD synergistically induced DNA damage in tumor cells (Fig. 6D and E). To further validate the induction of DNA damage and epigenetic alterations in vivo, we performed immunofluorescence staining for γH2AX and H3K27me3 in xenograft tumors. Combination treatment with methionine restriction and GSK126 resulted in increased γH2AX and decreased H3K27me3 signals, compared to either monotherapy or control (Supplementary Fig. 4A). These results are consistent with enhanced DNA damage and H3K27 methylation loss upon dual inhibition of MAT2A and EZH2. To further confirm the regulatory relationship between MAT2A and EZH2 in vivo, we performed xenograft assays using EZH2-overexpressing HOS cells. Compared to vector controls, tumors derived from EZH2-OE cells showed diminished response to PF-9366 treatment, with significantly larger tumor volumes and weights (Fig. 6F and G). Body weight remained unchanged across groups (Fig. 6H). Histological analysis revealed that EZH2 overexpression restored H3K27me3 levels and suppressed γH2AX and cleaved caspase-3 expression, indicating reduced DNA damage and apoptosis (Supplementary Fig. 4B). These results support the notion that EZH2 upregulation compromises the tumor-suppressive effects of MAT2A inhibition in vivo, consistent with in vitro findings. In conclusion, the combination of EZH2 inhibitor and methionine-restricted diet exhibited a synergistic effect in suppressing osteosarcoma growth in vivo.

4. Discussion

As an essential amino acid, methionine plays a critical role in tumor biology. Accumulating evidence indicates that malignant cells exhibit heightened methionine dependency to sustain proliferation, often outcompeting T cells for methionine uptake within the tumor microenvironment [42–46]. While methionine deprivation has emerged as a potential therapeutic strategy [27,37,47], key mechanistic insights remain limited—particularly the lack of single-cell transcriptomic evidence directly linking methionine metabolism to malignant progression. Notably, activated methionine pathways have been reported in esophageal squamous cell carcinoma [48], lung cancer [49], and hepatocellular carcinoma [50], yet their functional significance in other malignancies requires systematic investigation. Our study addresses this gap by revealing upregulated methionine metabolism in OS cells through single-cell transcriptomic profiling. This metabolic reprogramming appears functionally critical, as demonstrated by two complementary lines of evidence: First, methionine restriction significantly suppresses colorectal cancer growth in both preclinical models [37,47] and clinical observations [51]. Second, our metabolite screening directly correlates methionine availability with enhanced OS cell viability. These findings collectively position methionine metabolism as a promising therapeutic target, with microenvironmental methionine depletion strategies showing broad antitumor efficacy across malignancies [51].

MAT2A, a key enzyme driving methionine metabolism through its catalytic role in methionine adenosyltransferase cycling, has emerged as a critical oncogenic driver across malignancies. Clinical analyses reveal consistent MAT2A upregulation in multiple tumor types compared with normal tissues, including gastric cancer [52], lung adenocarcinoma

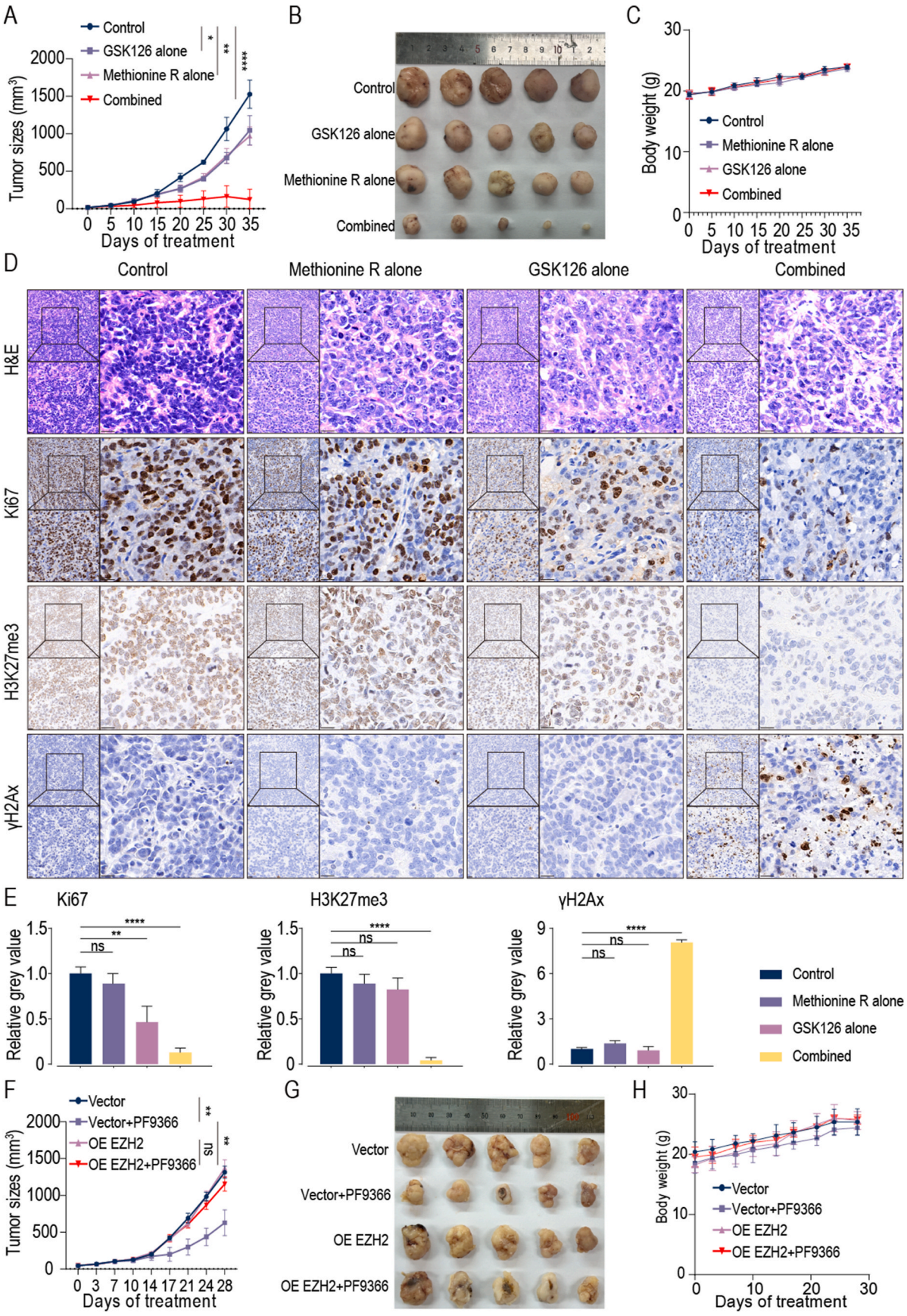

(caption on next page)

Fig. 6. The synergistic effect of EZH2 inhibitor and methionine-restricted diet suppresses osteosarcoma growth in vivo. (A) Tumor volume growth curves of subcutaneous tumor models in mice treated with EZH2 inhibitor (GSK126) and MAT2A inhibitor (PF-9366), *: $p < 0.05$, **: $p < 0.01$, ****: $p < 0.0001$. Biological replicates = 5. (B) Representative tumor images from different treatment groups. (C) Body weight changes in mice over time across treatment groups. Biological replicates = 5. (D) Immunohistochemistry (IHC) staining of Ki67, H3K27me3, and γH2AX, as well as H&E staining of tumor tissues. Scale bar: 20 μm. (E) Quantification of relative IHC staining intensity, ns: $p > 0.05$, **: $p < 0.01$, ****: $p < 0.0001$. Technical replicates = 5. (F) Tumor volume growth curves of subcutaneous tumor models in mice treated with EZH2 Overexpression and MAT2A inhibitor (PF-9366), ns: $p < 0.05$, **: $p < 0.01$. Biological replicates = 5. (G) Representative tumor images from different treatment groups. (H) Body weight changes in mice over time across treatment groups. Biological replicates = 5.

[53], and breast cancer where its cytoplasmic overexpression correlates with enhanced invasiveness [54]. Prognostically, elevated MAT2A expression portends poorer survival outcomes in hepatocellular carcinoma [55], gynecological malignancies (cervical/ovarian/endometrial cancers) [56], and gastrointestinal tumors (gastric/colorectal cancers) [57]. This pattern extends to osteosarcoma, where our cohort analysis establishes high MAT2A expression as an independent predictor of adverse prognosis.

The therapeutic promise of MAT2A targeting is underscored by preclinical evidence spanning diverse models: Genetic ablation via CRISPR-Cas9 suppresses hepatocellular carcinoma progression [58], RNA interference-mediated knockdown attenuates prostate cancer growth in vitro and in vivo, albeit with subtype-dependent efficacy [59], Pharmacological inhibitors demonstrate potent anti-tumor activity in colorectal cancer models [60].

However, intertumoral and intratumoral heterogeneity in MAT2A dependency poses therapeutic challenges. Mechanistic studies attribute this variability to two non-exclusive mechanisms: (1) genetic/epigenetic heterogeneity across molecular subtypes [55,59], and (2) compensatory MAT2A upregulation through negative feedback loops upon inhibitor exposure [41,61]. Interestingly, we observed a dose-dependent increase in MAT2A protein levels upon PF-9366 treatment. This effect may reflect a compensatory feedback mechanism triggered by MAT2A inhibition and SAM depletion. Previous work has shown that PF-9366 acts as an allosteric inhibitor that suppresses MAT2A enzymatic activity without necessarily reducing its protein stability [41]. The increase in MAT2A expression may therefore represent a feedback response aimed at restoring SAM homeostasis. Despite the elevated protein levels, our downstream analyses revealed reduced H3K27me3 and increased DNA damage signals, indicating that MAT2A activity was effectively inhibited at the functional level. Our functional studies in osteosarcoma models support the primacy of intrinsic genetic determinants. Notably, MAT2A inhibitor-sensitive cell lines (143B, U2-OS) exhibited paradoxical MAT2A upregulation during treatment, suggesting the absence of robust compensatory adaptation—a finding that reinforces the need for biomarker-guided patient stratification. Moreover, in this study, we prioritized pharmacological inhibition of MAT2A using PF-9366 for histone modification analyses, as this approach reflects a clinically relevant strategy with potential for translational application. While genetic knockdown confirmed the functional role of MAT2A in tumor growth, small-molecule inhibition allowed us to explore the epigenetic consequences of a therapeutic modality that could be more readily applied in future clinical settings.

To further investigate the differential sensitivity to MAT2A inhibition, we analyzed two OS cell lines with distinct responses and identified EZH2-mediated upregulation of H3K27me3 as a key factor contributing to drug resistance. However, there are certain limitations to this study. Firstly, we focused primarily on the 143B and HOS/MNNG cell lines and did not examine other OS cell lines, such as U2-OS and HOS, which may exhibit distinct regulatory mechanisms. Additionally, while EZH2 was identified as an enzyme responsible for regulating H3K27me3, it is possible that other enzymes also contribute to this process. Therefore, future studies should aim to further elucidate the regulatory mechanisms of H3K27me3 and its involvement in MAT2A inhibitor resistance in OS. Moreover, further exploration of the clinical potential of a combined targeting strategy against both EZH2 and MAT2A is warranted.

Author Contributions

Conceptualization, W.S., Y.Q.H., D.Q.Z., C.X.Y. and H.R.M.; Methodology, H.R.M., Y.N.T. and B.H.Y.; Validation, Y.Q.H., H.R.M.; Formal Analysis, B.H.Y. and H.R.M.; Investigation, B.H.Y. and H.R.M.; Resources, W.S., D.Q.Z, Y.Q.H., Y.F.J. and Z.D.C.; Data Curation, H.R.M., H.Y.W., B.H.Y. and Y.N.T.; Writing – Original Draft, B.H.Y., H.R.M., and Y.N.T.; Writing – Review & Editing, all authors; Visualization, H.R.M. and B.H.Y.; Supervision, Z.Y.W., X.Y.Y and B.H.Y; Project Administration, Z.Y.W. and Y.F.J.; Funding Acquisition, Z.D.C., H.R.M., Y.Q.H. and W.S.

Ethical statement

This study was approved by the Institutional Research Ethics Committee of Shanghai General Hospital, Shanghai Jiao Tong University School of Medicine (Approval No. 2021KY103). All animal experiments were conducted in accordance with the guidelines and protocols approved by the Laboratory Animal Welfare & Ethics Committee of Shanghai General Hospital.

Declaration of interests

The authors declare that the research was conducted in the absence of any commercial or financial relationships that could be construed as a potential conflict of interest.

Acknowledgements

This research was supported by the National Natural Science Foundation of China (Grants No. 82272773, 82373177, 82404064 and 82172366) and Shanghai Municipal Health Commission Clinical Research Program (Grants No. 202240215). We are grateful to Professor Yujie Tang (Shanghai Jiao Tong University School of Medicine, China) for her valuable suggestions and feedback. We appreciate Mingxi Li (Apeiron Therapeutics, China).

Renhong Tang (State Key Laboratory of Neurology and Oncology Drug Development, Nanjing, China),Feng Tang (State Key Laboratory of Neurology and Oncology Drug Development, Nanjing, China) and Zhen Li (State Key Laboratory of Neurology and Oncology Drug Development, Nanjing, China) for their contributions to this research. We appreciate to Qi Zhang (Shanghai Jiao Tong University School of Medicine, China) and to Doctor Yan Yan (Naval Medical University, China) for their insightful advice and assistance.

Appendix A. Supplementary data

Supplementary data to this article can be found online at https://doi.org/10.1016/j.jot.2025.09.007.

References

[1] Kansara M, Teng MW, Smyth MJ, Thomas DM. Translational biology of osteosarcoma. Nat Rev Cancer 2014;14(11):722–35.
[2] Beird HC, Bielack SS, Flanagan AM, Gill J, Heymann D, Janeway KA, et al. Osteosarcoma. Nat Rev Dis Primers 2022;8(1):77.
[3] Misaghi A, Goldin A, Awad M, Kulidjian AA. Osteosarcoma: a comprehensive review. SICOT J 2018;4:12.

[4] Whelan JS, Davis LE. Osteosarcoma, chondrosarcoma, and chordoma. J Clin Oncol 2018;36(2):188–93.
[5] Hoeijmakers JH. DNA damage, aging, and cancer. N Engl J Med 2009;361(15):1475–85.
[6] Quinet A, Tirman S, Cybulla E, Meroni A, Vindigni A. To skip or not to skip: choosing repriming to tolerate DNA damage. Mol Cell 2021;81(4):649–58.
[7] Costantino L, Koshland D. The yin and yang of R-loop biology. Curr Opin Cell Biol 2015;34:39–45.
[8] Santos-Pereira JM, Aguilera A. R loops: new modulators of genome dynamics and function. Nat Rev Genet 2015;16(10):583–97.
[9] Skourti-Stathaki K, Proudfoot NJ. A double-edged sword: r loops as threats to genome integrity and powerful regulators of gene expression. Genes Dev 2014;28(13):1384–96.
[10] Tresini M, Warmerdam DO, Kolovos P, Snijder L, Vrouwe MG, Demmers JA, et al. The core spliceosome as target and effector of non-canonical ATM signalling. Nature 2015;523(7558):53–8.
[11] Adam S, Rossi SE, Moatti N, De Marco Zompit M, Xue Y, Ng TF, et al. The CIP2A-TOPBP1 axis safeguards chromosome stability and is a synthetic lethal target for BRCA-Mutated cancer. Nat Cancer 2021;2(12):1357–71.
[12] Wei X, Yang J, Adair SJ, Ozturk H, Kuscu C, Lee KY, et al. Targeted CRISPR screening identifies PRMT5 as synthetic lethality combinatorial target with gemcitabine in pancreatic cancer cells. Proc Natl Acad Sci U S A 2020;117(45):28068–79.
[13] Groelly FJ, Fawkes M, Dagg RA, Blackford AN, Tarsounas M. Targeting DNA damage response pathways in cancer. Nat Rev Cancer 2023;23(2):78–94.
[14] Goldstein M, Kastan MB. The DNA damage response: implications for tumor responses to radiation and chemotherapy. Annu Rev Med 2015;66:129–43.
[15] Dibitetto D, Marshall S, Sanchi A, Liptay M, Badar J, Lopes M, et al. DNA-PKcs promotes fork reversal and chemoresistance. Mol Cell 2022;82(20):3932–39342 e6.
[16] Gardner EE, Lok BH, Schneeberger VE, Desmeules P, Miles LA, Arnold PK, et al. Chemosensitive relapse in small cell lung cancer proceeds through an EZH2-SLFN11 axis. Cancer Cell 2017;31(2):286–99.
[17] Landau DA, Carter SL, Stojanov P, McKenna A, Stevenson K, Lawrence MS, et al. Evolution and impact of subclonal mutations in chronic lymphocytic leukemia. Cell 2013;152(4):714–26.
[18] Waddington CH. The epigenotype. 1942. Int J Epidemiol 2012;41(1):10–3.
[19] Hanahan D, Weinberg RA. Hallmarks of cancer: the next generation. Cell 2011;144(5):646–74.
[20] Chang SL, Lee CW, Yang CY, Lin ZC, Peng KT, Liu SC, et al. IOX-1 suppresses metastasis of osteosarcoma by upregulating histone H3 lysine trimethylation. Biochem Pharmacol 2023;210:115472.
[21] Jiang Y, Li F, Gao B, Ma M, Chen M, Wu Y, et al. KDM6B-mediated histone demethylation of LDHA promotes lung metastasis of osteosarcoma. Theranostics 2021;11(8):3868–81.
[22] Yadav P, Subbarayalu P, Medina D, Nirzhor S, Timilsina S, Rajamanickam S, et al. M6A RNA methylation regulates histone ubiquitination to support cancer growth and progression. Cancer Res 2022;82(10):1872–89.
[23] Zhou Y, Yang D, Yang Q, Lv X, Huang W, Zhou Z, et al. Single-cell RNA landscape of intratumoral heterogeneity and immunosuppressive microenvironment in advanced osteosarcoma. Nat Commun 2020;11(1):6322.
[24] Wang Y, Wang R, Zhang S, Song S, Jiang C, Han G, et al. iTALK: an R package to characterize and illustrate intercellular communication. bioRxiv 2019:507871.
[25] Liu Y, He M, Tang H, Xie T, Lin Y, Liu S, et al. Single-cell and spatial transcriptomics reveal metastasis mechanism and microenvironment remodeling of lymph node in osteosarcoma. BMC Med 2024;22(1):200.
[26] Thomas DD, Lacinski RA, Lindsey BA. Single-cell RNA-Seq reveals intratumoral heterogeneity in osteosarcoma patients: a review. J Bone Oncol 2023;39:100475.
[27] Mu H, Zhang Q, Zuo D, Wang J, Tao Y, Li Z, et al. Methionine intervention induces PD-L1 expression to enhance the immune checkpoint therapy response in MTAP-Deleted osteosarcoma. Cell Rep Med 2025:101977.
[28] Dobin A, Davis CA, Schlesinger F, Drenkow J, Zaleski C, Jha S, et al. STAR: ultrafast universal RNA-Seq aligner. Bioinformatics 2013;29(1):15–21 [eng].
[29] Liao Y, Smyth GK, Shi W. featureCounts: an efficient general purpose program for assigning sequence reads to genomic features. Bioinformatics 2014;30(7):923–30 [eng].
[30] Love MI, Huber W, Anders S. Moderated estimation of fold change and dispersion for RNA-seq data with DESeq2. Genome Biol 2014;15(12):550 [eng].
[31] Durinck S, Spellman PT, Birney E, Huber W. Mapping identifiers for the integration of genomic datasets with the R/Bioconductor package biomaRt. Nat Protoc 2009;4(8):1184–91 [eng].
[32] Durinck S, Moreau Y, Kasprzyk A, Davis S, De Moor B, Brazma A, et al. BioMart and bioconductor: a powerful link between biological databases and microarray data analysis. Bioinformatics 2005;21(16):3439–40 [eng].
[33] Yu G, Wang LG, Han Y, He QY. clusterProfiler: an R package for comparing biological themes among gene clusters. OMICS 2012;16(5):284–7 [eng].
[34] Subramanian A, Tamayo P, Mootha VK, Mukherjee S, Ebert BL, Gillette MA, et al. Gene set enrichment analysis: a knowledge-based approach for interpreting genome-wide expression profiles. Proc Natl Acad Sci U S A 2005;102(43):15545–50 [eng].
[35] Liberzon A, Subramanian A, Pinchback R, Thorvaldsdóttir H, Tamayo P, Mesirov JP. Molecular signatures database (MSigDB) 3.0. Bioinformatics 2011;27(12):1739–40 [eng].
[36] Liberzon A, Birger C, Thorvaldsdóttir H, Ghandi M, Mesirov JP, Tamayo P. The molecular signatures database (MSigDB) hallmark gene set collection. Cell Syst 2015;1(6):417–25 [eng].
[37] Gao X, Sanderson SM, Dai Z, Reid MA, Cooper DE, Lu M, et al. Dietary methionine influences therapy in mouse cancer models and alters human metabolism. Nature 2019;572(7769):397–401.
[38] Ducker GS, Rabinowitz JD. One-carbon metabolism in health and disease. Cell Metab 2017;25(1):27–42.
[39] Sun Q, Huang M, Wei Y. Diversity of the reaction mechanisms of SAM-Dependent enzymes. Acta Pharm Sin B 2021;11(3):632–50.
[40] Xing Z, Tu BP. Mechanisms and rationales of SAM homeostasis. Trends Biochem Sci 2025;50(3):242–54.
[41] Quinlan CL, Kaiser SE, Bolanos B, Nowlin D, Grantner R, Karlicek-Bryant S, et al. Targeting S-adenosylmethionine biosynthesis with a novel allosteric inhibitor of Mat2A. Nat Chem Biol 2017;13(7):785–92.
[42] Bin P, Wang C, Zhang H, Yan Y, Ren W. Targeting methionine metabolism in cancer: opportunities and challenges. Trends Pharmacol Sci 2024;45(5):395–405.
[43] Kaiser P. Methionine dependence of cancer. Biomolecules 2020;10(4).
[44] Sanderson SM, Gao X, Dai Z, Locasale JW. Methionine metabolism in health and cancer: a nexus of diet and precision medicine. Nat Rev Cancer 2019;19(11):625–37.
[45] Tassinari V, Jia W, Chen WL, Candi E, Melino G. The methionine cycle and its cancer implications. Oncogene 2024;43(48):3483–8.
[46] Bian Y, Li W, Kremer DM, Sajjakulnukit P, Li S, Crespo J, et al. Cancer SLC43A2 alters T cell methionine metabolism and histone methylation. Nature 2020;585(7824):277–82.
[47] Li T, Tan YT, Chen YX, Zheng XJ, Wang W, Liao K, et al. Methionine deficiency facilitates antitumour immunity by altering m(6)A methylation of immune checkpoint transcripts. Gut 2023;72(3):501–11.
[48] Jin X, Liu L, Liu D, Wu J, Wang C, Wang S, et al. Unveiling the methionine cycle: a key metabolic signature and NR4A2 as a methionine-responsive oncogene in esophageal squamous cell carcinoma. Cell Death Differ 2024;31(5):558–73.
[49] Qian J, Olbrecht S, Boeckx B, Vos H, Laoui D, Etlioglu E, et al. A pan-cancer blueprint of the heterogeneous tumor microenvironment revealed by single-cell profiling. Cell Res 2020;30(9):745–62.
[50] Li F, Liu P, Mi W, Li L, Anderson NM, Lesner NP, et al. Blocking methionine catabolism induces senescence and confers vulnerability to GSK3 inhibition in liver cancer. Nat Cancer 2024;5(1):131–46.
[51] Zhou S, Lin Y, Zhao Z, Lai Y, Lu M, Shao Z, et al. Targeted deprivation of methionine with engineered salmonella leads to oncolysis and suppression of metastasis in broad types of animal tumor models. Cell Rep Med 2023;4(6):101070.
[52] Yang C, Ou Y, Zhou Q, Liang Y, Li W, Chen Y, et al. Methionine orchestrates the metabolism vulnerability in cisplatin resistant bladder cancer microenvironment. Cell Death Dis 2023;14(8):525.
[53] Ma M, Kong P, Huang Y, Wang J, Liu X, Hu Y, et al. Activation of MAT2A-ACSL3 pathway protects cells from ferroptosis in gastric cancer. Free Radic Biol Med 2022;181:288–99.
[54] Chu PY, Wu HJ, Wang SM, Chen PM, Tang FY, Chiang EI. MAT2A localization and its independently prognostic relevance in breast cancer patients. Int J Mol Sci 2021;22(10).
[55] Villa E, Sahu U, O'Hara BP, Ali ES, Helmin KA, Asara JM, et al. mTORC1 stimulates cell growth through SAM synthesis and m(6)A mRNA-dependent control of protein synthesis. Mol Cell 2021;81(10):2076–20793 e9.
[56] Li JT, Yang H, Lei MZ, Zhu WP, Su Y, Li KY, et al. Dietary folate drives methionine metabolism to promote cancer development by stabilizing MAT IIA. Signal Transduct Targeted Ther 2022;7(1):192.
[57] Frau M, Feo F, Pascale RM. Pleiotropic effects of methionine adenosyltransferases deregulation as determinants of liver cancer progression and prognosis. J Hepatol 2013;59(4):830–41.
[58] Hung MH, Lee JS, Ma C, Diggs LP, Heinrich S, Chang CW, et al. Tumor methionine metabolism drives T-cell exhaustion in hepatocellular carcinoma. Nat Commun 2021;12(1):1455.
[59] Cacciatore A, Shinde D, Musumeci C, Sandrini G, Guarrera L, Albino D, et al. Epigenome-wide impact of MAT2A sustains the androgen-indifferent state and confers synthetic vulnerability in ERG fusion-positive prostate cancer. Nat Commun 2024;15(1):6672.
[60] Yu Z, Kuang Y, Xue L, Ma X, Li T, Yuan L, et al. SCR-7952, a highly selective MAT2A inhibitor, demonstrates synergistic antitumor activities in combination with the S-adenosylmethionine-competitive or the methylthioadenosine-cooperative protein arginine methyltransferase 5 inhibitors in methylthioadenosine phosphorylase-deleted tumors. MedComm 2024;5(10):e705(2020).
[61] Konteatis Z, Travins J, Gross S, Marjon K, Barnett A, Mandley E, et al. Discovery of AG-270, a first-in-class oral MAT2A inhibitor for the treatment of tumors with homozygous MTAP deletion. J Med Chem 2021;64(8):4430–49.